Chemical Science

ROYAL SOCIETY OF CHEMISTRY

EDGE ARTICLE

View Article Online
View Journal

Check for updates

Cite this: DOI: 10.1039/d6sc00819d

All publication charges for this article have been paid for by the Royal Society of Chemistry

Received 29th January 2026
Accepted 9th April 2026

DOI: 10.1039/d6sc00819d

rsc.li/chemical-science

# Linker desymmetrisation directs low-polar cages in an anion-pillared MOF for acetylene and ethylene purification from ternary mixtures

Jun-Jie Wu,[a] Peng-Dan Zhang,*[ac] Xue-Qian Wu,*[a] Shuai-Hao Huang,[a] Wen-Wen Dong,[a] Ya-Pan Wu[a] and Dong-Sheng Li*[ab]

Anion-pillared metal–organic frameworks (APMOFs) constitute a promising class of porous adsorbents, yet precise organization of anionic groups to maximize their strong electronegative character while circumventing highly polar pore environments and high adsorption enthalpies remains a substantial challenge. Here, we report a novel APMOF, CTGU-45, featuring an atypical low-polar cage surface distinct from reported APMOFs and then explore its $C_2H_2$ and $C_2H_4$ purification from ternary $C_2H_2/CO_2/CH_4$ and $C_2H_2/C_2H_4/C_2H_6$ mixtures. Theoretical calculation results revealed the mechanisms of simultaneous recognition of $C_2H_2$ and $C_2H_6$ molecules from $C_2$ hydrocarbons: the $SiF_6^{2-}$ pillars provide strong binding sites for $C_2H_2$ *via* C–H⋯F hydrogen bonds, while the TIB-derived low-polar surface offers an optimal environment for $C_2H_6$ adsorption through synergistic C–H⋯π and C–H⋯N interactions. Dynamic breakthrough experiments further confirm the efficient separation of $C_2H_2/CO_2$, $C_2H_2/CO_2/CH_4$, and notably one-step production of polymer-grade $C_2H_4$ (≥99.95%, 9.57 L $kg^{-1}$) from ternary $C_2H_2/C_2H_4/C_2H_6$ mixtures with low regeneration energy. Crucially, CTGU-45 can be synthesized on a 500 mL scale with retained performance, underscoring its practical feasibility and laying a solid foundation for future industrial applications.

## Introduction

Acetylene ($C_2H_2$) and ethylene ($C_2H_4$) are pivotal feedstocks in the chemical industry.[1] $C_2H_2$ is typically generated by partial oxidation of methane ($CH_4$) or thermal cracking of hydrocarbons, which co-produces significant amounts of carbon dioxide ($CO_2$).[2–5] Similarly, $C_2H_4$ is obtained *via* steam cracking or ethane ($C_2H_6$) dehydrogenation, where $C_2H_6$ and trace $C_2H_2$ will unavoidably be produced as by-products.[6,7] These impurities severely compromise the purity and productivity of polymer-grade $C_2H_4$ or high-purity $C_2H_2$, necessitating highly efficient separation processes.[8,9] However, the similar physicochemical properties of these gas molecules make separations ($C_2H_2/CO_2/CH_4$, $C_2H_2/C_2H_4/C_2H_6$) particularly difficult (Table S2). Conventional methods like catalytic hydrogenation and cryogenic distillation are complex and energy-intensive, thus driving the urgent need for efficient, alternative separation technologies.[10–12]

Adsorptive separation using porous materials presents a promising, energy-efficient alternative to traditional cryogenic distillation.[13–16] Among various adsorbents, metal–organic frameworks (MOFs) have garnered immense attention due to their designable pore structures and tunable surface functionalities. In particular, anion-pillared MOFs (APMOFs) have emerged as an important subclass of MOF adsorbents. These materials utilize inorganic anions (*e.g.*, $SiF_6^{2-}$, $GeF_6^{2-}$, $NbOF_5^{2-}$, $MoO_4^{2-}$) as structural pillars to construct robust frameworks with strong electrostatic potential fields and abundant electronegative atoms that act as hydrogen-bond (H-bond) acceptors, enabling highly selective recognition of $C_2H_2$ with strong positive H atoms and $C_2H_6$ with more H atoms. Initially, APMOFs are constructed from linear bidentate ligands to form one-dimensional (1D) channels.[17–20] The subsequent introduction of tri- and tetra-dentate ligands created more open APMOFs with a "cage + window" structure, which provides high capacity from large cages and high selectivity from narrow windows. Certainly, these APMOFs have been considered as valuable candidates capable of addressing the "trade-off" between capacity and selectivity in gas separation.

To date, only three highly symmetrical tridentate modules (Tripp, 2,4,6-tris(4-pyridyl)pyridine; TPA, tri(pyridin-4-yl)amine; and TPT, 2,4,6-tri(4-pyridyl)-1,3,5-triazine) have been successfully employed to construct APMOFs and used for gas separation, such as $C_2H_2/CO_2$, $CO_2/N_2$, $C_3H_4/C_3H_6$, Xe/Kr, and $C_6$

---

[a] College of Materials and Chemical Engineering, China Three Gorges University, Yichang 443002, P. R. China. E-mail: dana929@163.com; wuxueqiansnail@163.com; lidongsheng1@126.com

[b] Hubei Three Gorges Laboratory, Yichang 443007, Hubei, P. R. China

[c] College of Hydraulic & Environmental Engineering, China Three Gorges University, Yichang 443002, P. R. China

hydrocarbons. These ligands share critical structural features: their terminal coordinating units are all pyridine rings, which enforce a nearly ideal equilateral triangular arrangement of the three coordination N atoms. Although limited rotation of the pyridine rings is possible, the spatial positions of these key N donors remain essentially fixed, enabling a predictable assembly of frameworks. Interestingly, replacing the terminal pyridyl moiety with less symmetric imidazole rings would introduce significant conformational flexibility. The free rotation around the C–N single bonds linking the central benzene ring to the imidazole arms results in variable spatial orientations of the coordination N atoms, thereby breaking the inherent topological symmetry and creating opportunities for constructing APMOFs with unique pores. Moreover, certain challenging separations, *e.g.*, one-step $C_2H_4$ purification from ternary $C_2$ mixtures, are seldom realized in APMOFs owing to intrinsic polarity mismatches, suggesting that a reconfiguration of functional sites within APMOFs is required. Since the coordination geometry and configuration of inorganic anions are relatively well-defined, the linker desymmetrisation offers a powerful means to systematically reorganize the functional sites within APMOFs. By changing the symmetry of the organic linkers, it becomes possible to create frameworks in which the chemical environment around each coordination site can be independently tuned. This controlled asymmetry allows for the introduction of complementary binding sites, modulation of local polarity, and the rational design of preferential adsorption domains, ultimately enhancing the selectivity and efficiency of challenging gas separations.

Keep this in mind, herein, by utilizing a tridentate TIB linker (1,3,5-tri(1*H*-imidazol-1-yl)benzene) with $C_3$ symmetry, a novel $SiF_6^{2-}$ anion hybrid Cu-MOF (SIFSIX-Cu-TIB, CTGU-45, CTGU = China Three Gorges University) has been successfully constructed. Single-crystal X-ray diffraction (SCXRD) analysis reveals that the activated CTGU-45 features uniform cage-like pores with an internal cage diameter of approximately 7.6 Å and a pore window size of about 6.5 Å. In contrast to most reported cage-structured APMOFs, the main pore surface of CTGU-45 is defined solely by TIB ligands and Cu(II) nodes, resulting in a low-polar pore environment that provides optimized adsorption space for $C_2H_6$ molecules. This establishes a foundation for the one-step production of high-purity $C_2H_4$ from ternary $C_2$ hydrocarbon mixtures ($C_2H_2/C_2H_4/C_2H_6$). Meanwhile, the marginalized F atoms of the inorganic $SiF_6^{2-}$ pillars serve as strong basic sites, engaging in pronounced interactions with the acidic H atoms of $C_2H_2$, thereby facilitating efficient $C_2H_2/CO_2$, $C_2H_2/CO_2/CH_4$, and $C_2H_2/C_2H_4$ separations (Scheme 1). The outstanding separation performances, as well as the underlying adsorbate–adsorbent interactions, have been comprehensively verified by a combination of experimental static adsorption/dynamic breakthrough tests and theoretical calculations. This work not only creates CTGU-45 as an efficient adsorbent for challenging $C_2$ hydrocarbons separation but also demonstrates the great potential of ligand engineering to break the inherent limitations of conventional APMOFs, opening up new avenues for developing advanced adsorbents.

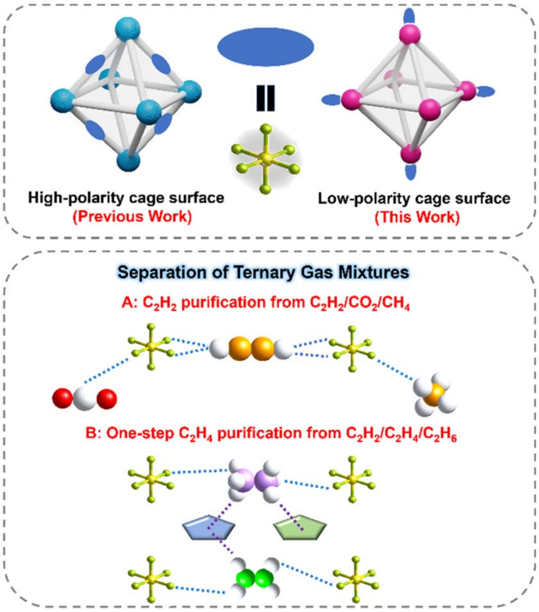

Scheme 1 Comparison of cage polarity and using CTGU-45 for the separation of ternary gas mixtures. Unlike the high-polarity cages in typical APMOFs (left), CTGU-45 (right) features a low-polarity cage surface constructed exclusively from $Cu^{2+}$ nodes and TIB ligands. The $SiF_6^{2-}$ pillars served as strong basic sites for $C_2H_2$, and non-polar cage surfaces provided the interaction for $C_2H_6$, which promotes CTGU-45 to realize the effective $C_2H_2$ and $C_2H_4$ purification from $C_2H_2/CO_2/CH_4$ and $C_2H_2/C_2H_4/C_2H_6$ mixtures, respectively.

## Results and discussion

Blue octahedral single crystals of CTGU-45 were successfully synthesized by reacting $Cu(OAc)_2 \cdot H_2O$ and TIB ligand in a mixed solvent of *N*,*N*-dimethylacetamide (DMA)/$H_2O$, with $HBF_4$ added in a sealed glass tube (Fig. S3). SCXRD analysis revealed that CTGU-45 crystallizes in a three-dimensional (3D) framework with the cubic system space group $Pm\bar{3}n$. Each Cu(II) cation is coordinated in a square-planar geometry by four N atoms from imidazole groups of four distinct tridentate TIB ligands (Fig. S2). The $SiF_6^{2-}$ anions as 2-connected nodes occupy the two axial positions to complete the octahedral coordination. Notably, the $SiF_6^{2-}$ anions originated from the *in situ* etching of the borosilicate glass vessel by HF (from $HBF_4$ hydrolysis). Due to the free rotation of the C–N bonds between the central benzene and imidazole moieties, the TIB ligands in CTGU-45 exhibit substantial disorder. Upon removal of the minor disordered components, the real structure shows a uniform cage-like architecture with a pore diameter of approximately 7.6 Å (Fig. 1f). Each incomplete octahedral cage displays four identical triangular windows consisting of three TIB linkers and three $Cu^{2+}$ ions. The effective aperture of these windows, after considering the van der Waals radii of H atoms, is only about 6.5 Å, allowing the entry of $C_1$–$C_2$ hydrocarbon molecules (Fig. S1). These cages are further linked by $SiF_6^{2-}$ anion, whose F atoms act as potential Lewis basic sites, which may work synergistically with the confined space and aromatic

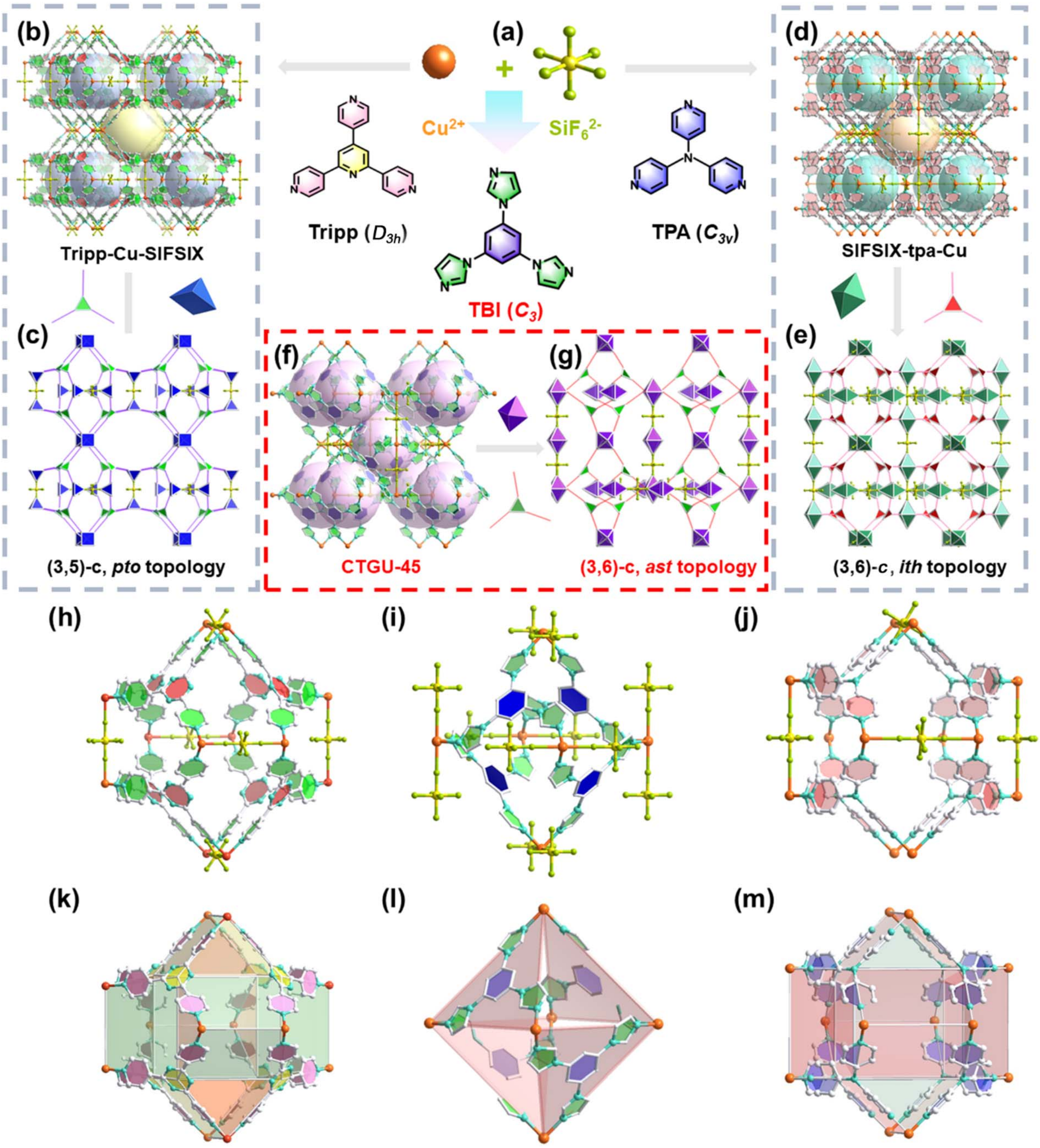

Fig. 1 (a) The frameworks of Tripp-Cu-SIFSIX, SIFSIX-Cu-TPA, and CTGU-45 are based on the assembly of $SiF_6^{2-}$, $Cu^{2+}$, and Tripp/TPA/TIB ligands, respectively. (b and c) The crystal structure and (3,5)-connected ***pto*** topology of Tripp-Cu-SIFSIX. (d and e) Crystal structure and (3,6)-connected *i*th topology of SIFSIX-Cu-TPA. (f and g) The crystal structure and (3,6)-connected topology of CTGU-45. Cage structures within (h)/(k) Tripp-Cu-SIFSIX, (i)/(l) CTGU-45, and (j)/(m) SIFSIX-Cu-TPA. H atoms are omitted for clarity.

surface to enhance the binding of gas molecules. In contrast to most reported APMOFs, which typically consist of bidentate ligands and anion pillars forming 1D linear channels (*e.g.*, SIFSIX-1-Cu,[21] SIFSIX-3-Ni[22]), the structure presented here features a well-defined windowed cage architecture. Furthermore, APMOFs constructed from tridentate ligands are exceptionally rare. To our knowledge, only three tridentate ligands (Tripp, TPA, and TPT) have been reported for constructing APMOFs, such as Tripp-Cu-SIFSIX[23] (Fig. 1b) and SIFSIX-Cu-TPA (Fig. 1d),[24] both of which exhibit two distinct types of cages. Tripp-Cu-SIFSIX displays octahedra cages (∼7.2 Å) and icositetrahedron cages (∼8.9 Å), while SIFSIX-Cu-TPA possesses icosahedral cages (∼6.0 Å) and tetrahedral cages (∼4.7 Å). Though the pyridine rings of Tripp ($D_{3h}$, excluding the non-coordinating pyridine N atom) and TPA ($C_{3v}$) ligands could rotate around C(pyridine)–C(pyridine) or N–C(benzene) single bonds, their three pyridyl N donors were locked into a fixed, equilateral triangular geometry. In contrast, the rotation of C(benzene)–N(imidazole) bonds in the TIB ($C_3$) linkers results in dynamic positions of coordination imidazole N atoms, breaking the perfect symmetry, as presented in Fig. 1a and S4. Such ligand asymmetry easily leads to a distorted coordination geometry and complicates the crystallization process, hindering the predictable assembly of conventional networks. Concretely, in the Tripp-Cu-SIFSIX, SIFSIX-Cu-TPA, and CTGU-45, all the organic linkers act as 3-connected topological nodes with $D_{3h}$ (Tripp/TPA-node) and $C_3$ (TIB-node) symmetry, respectively. Meanwhile, the coordination numbers of $Cu^{2+}$ are either 5 or 6, exhibiting square pyramidal ($C_{4v}$) or octahedral ($D_{4h}$) coordination geometries. The combination of organic nodes and metal nodes ultimately gives rise to (3,5)-c or (3,6)-c topological frameworks in three APMOFs (Fig. 1c/g/e). It is noteworthy that although $Cu^{2+}$ acts as a 6-c node in both SIFSIX-Cu-TPA and CTGU-45, the four pyridine rings coordinated to the $Cu^{2+}$ center in the former exhibit relative dihedral angles close to 90°, whereas the four imidazole rings coordinated to $Cu^{2+}$ in the latter are severely twisted. This causes the 6-c nodes in CTGU-45 to link adjacent nodes in a more distorted fashion, breaking the $D_{4h}$ extension symmetry of the 6-c nodes observed in SIFSIX-Cu-TPA. This, together with the 3-c nodes with $C_3$ symmetry, facilitates the formation of a geometrically self-consistent fundamental cage-like network in the absence of $SiF_6^{2-}$ anions (Fig. S4). The foregoing analysis has validated the critical influence of ligand symmetry on the formation of anionic hybrid frameworks. Overall, compared to Tripp-Cu-SIFSIX and SIFSIX-Cu-TPA, CTGU-45 shares the common feature of incorporating $SiF_6^{2-}$ anions, whose electronegative F atoms serve as Lewis-basic sites for interacting with acidic H atoms of $C_2H_2$. However, a fundamental distinction lies in their pore architecture: in conventional APMOFs, the $SiF_6^{2-}$ anions are integral components that participate directly in cage formation, resulting in highly polar pore surfaces dominated by F atoms (Fig. 1h/k and j/m). In contrast, in CTGU-45, the pore cages are constructed exclusively by the TIB ligands and Cu(II) nodes, while the $SiF_6^{2-}$ anions merely serve as inter-cage pillars (determined by the topology, Fig. 1i/l). This unique arrangement creates a low-polar pore surface rich in aromatic rings and N atoms, which not only provides optimal van der Waals interactions with highly polarizable $C_2H_6$ molecules but also enables synergistic binding through multiple C–H⋯π and C–H⋯N interactions. This distinctive pore environment, combined with the selective C–H⋯F binding sites at the $SiF_6^{2-}$ pillars, allows CTGU-45 to achieve cooperative adsorption of both $C_2H_2$ and $C_2H_6$, thereby providing a robust foundation for one-step $C_2H_4$ purification from ternary mixtures. The phase purity of the as-synthesized CTGU-45 was confirmed by powder X-ray diffraction (PXRD), as the experimental pattern matches well with simulated ones (Fig. S5). The thermogravimetric analysis (TGA) revealed the high thermal stability of activated CTGU-45, which remains stable up to 350 °C (Fig. S6). The initial weight loss below 100 °C is ascribed to solvent removal, while the subsequent major loss above 350 °C corresponds to the decomposition of the MOF framework. The $N_2$ adsorption isotherm of CTGU-45 at 77 K displayed a typical Type I profile, and the corresponding HK pore size distribution suggested ultramicropores of 6.1 Å, collectively confirming its microporous characteristic. The $N_2$ adsorption uptake of 125.5 $cm^3\ g^{-1}$ at 1 kPa and the calculated BET surface area of 544.8 $m^2\ g^{-1}$ further corroborated its porous structure (Fig. 2a). Moreover, the experimental pore volume of CTGU-45 was calculated to be 0.21 $cm^3\ g^{-1}$, which is consistent with the theoretical value from crystal structure (0.24 $cm^3\ g^{-1}$). Combined with its excellent thermal stability, these integrated properties collectively endorse CTGU-45 as a highly promising adsorbent for gas separation applications.

Single-component adsorption isotherms of $CH_4$, $CO_2$ and $C_2$–$C_3$ hydrocarbons on CTGU-45 were measured at 273, 283 and 298 K (Fig. 2b, c and S7–S18). CTGU-45 exhibited an obviously preferential adsorption of $C_2H_2$ over $CO_2$ and $CH_4$, with an uptake of 2.83 mmol $g^{-1}$ at 298 K and 101 kPa, significantly exceeding those of $CO_2$ (1.64 mmol $g^{-1}$) and $CH_4$ (0.74 mmol $g^{-1}$). Notably, the uptakes of $C_2H_2$ (2.00 mmol $g^{-1}$) and $C_2H_6$ (1.88 mmol $g^{-1}$) are significantly higher than that of $C_2H_4$ (1.75 mmol $g^{-1}$) at 30 kPa, thus showing great potential for one-step $C_2H_4$ purification. The $C_2H_2$ uptake capacity of CTGU-45 is higher than that of many reported APMOFs, such as NBOFFIVE-dps-Cu (1.65 mmol $g^{-1}$),[25] sql-SIFSIX-bpe-Zn (1.79 mmol $g^{-1}$),[26] DICRO-4-Ni-I (1.92 mmol $g^{-1}$),[27] ZNU-15 (1.61 mmol $g^{-1}$),[28] BSF-2 (1.85 mmol $g^{-1}$),[29] and BSF-4 (2.38 mmol $g^{-1}$).[30]

Meanwhile, the $CO_2$ adsorption amount is markedly lower than that of top-performing APMOFs, including SIFSIX-Cu-TPA (4.79 mmol $g^{-1}$),[24] QDU-MOF-1 (5.70 mmol $g^{-1}$),[31] TIFSIX-2-Cu-I (4.3 mmol $g^{-1}$),[32] ZNU-9 (4.32 mmol $g^{-1}$),[33] and ZNU-12 (4.33 mmol $g^{-1}$).[34] According to the virial equation, the isosteric heat of adsorption ($Q_{st}$) values at near-zero loading for $C_2H_2$, $C_2H_4$, $C_2H_6$, $CO_2$, and $CH_4$ on CTGU-45 are 30.9, 25.8, 27.3, 28.0, and 20.9 kJ $mol^{-1}$, respectively (Fig. 2d and S24–S28). The higher $Q_{st}$ value for $C_2H_2$ and $C_2H_6$, consistent with the steeper slope of its single-component adsorption isotherm, indicates a stronger binding affinity between the framework and $C_2H_2$ and $C_2H_6$ molecules. Overall, except for ZNU-8 (27.2 kJ $mol^{-1}$)[33] and MPM-1-TIFSIX (30.1 kJ $mol^{-1}$),[35] CTGU-45 exhibits the lowest $Q_{st}$ value for $C_2H_2$ among reported APMOFs, which is significantly lower than that of QDU-MOF-1 (72.52 kJ $mol^{-1}$),[31] TIFSIX-17-Ni (48.3 kJ $mol^{-1}$),[36] NBOFFIVE-dps-Cu (53.6 kJ $mol^{-1}$),[37] SIFSIX-Cu-TPA (39.1 kJ $mol^{-1}$)[24] and so on (Fig. 2h). Given that only one APMOF (ZUL-100)[33] has been reported for $C_2H_4$ purification from $C_2$ mixtures, the $C_2H_6$ $Q_{st}$ value of CTGU-45 (27.3 kJ $mol^{-1}$) is not only lower than that of ZUL-100 (34.2 kJ $mol^{-1}$),[33] but also lower than those of most previously reported $C_2H_2/C_2H_6$-selective MOFs for one-step $C_2H_4$ purification, such as Zn-trz-ox (38.7 kJ $mol^{-1}$),[38] NUM-9 (35.8 kJ $mol^{-1}$),[39] Zn-atz-oba (30.0 kJ $mol^{-1}$),[4] TJT-100 (29.0 kJ $mol^{-1}$),[40] and BUT-321 (28.5 kJ $mol^{-1}$)[41] (Fig. 2i). This low $Q_{st}$ value ensures easy desorption and low-energy regeneration, which might significantly reduce the operating cost in practical separation cycles.

In addition, since practical gas separation is a non-equilibrium process, the kinetic adsorption behavior should be evaluated synchronously. Therefore, we studied the kinetic

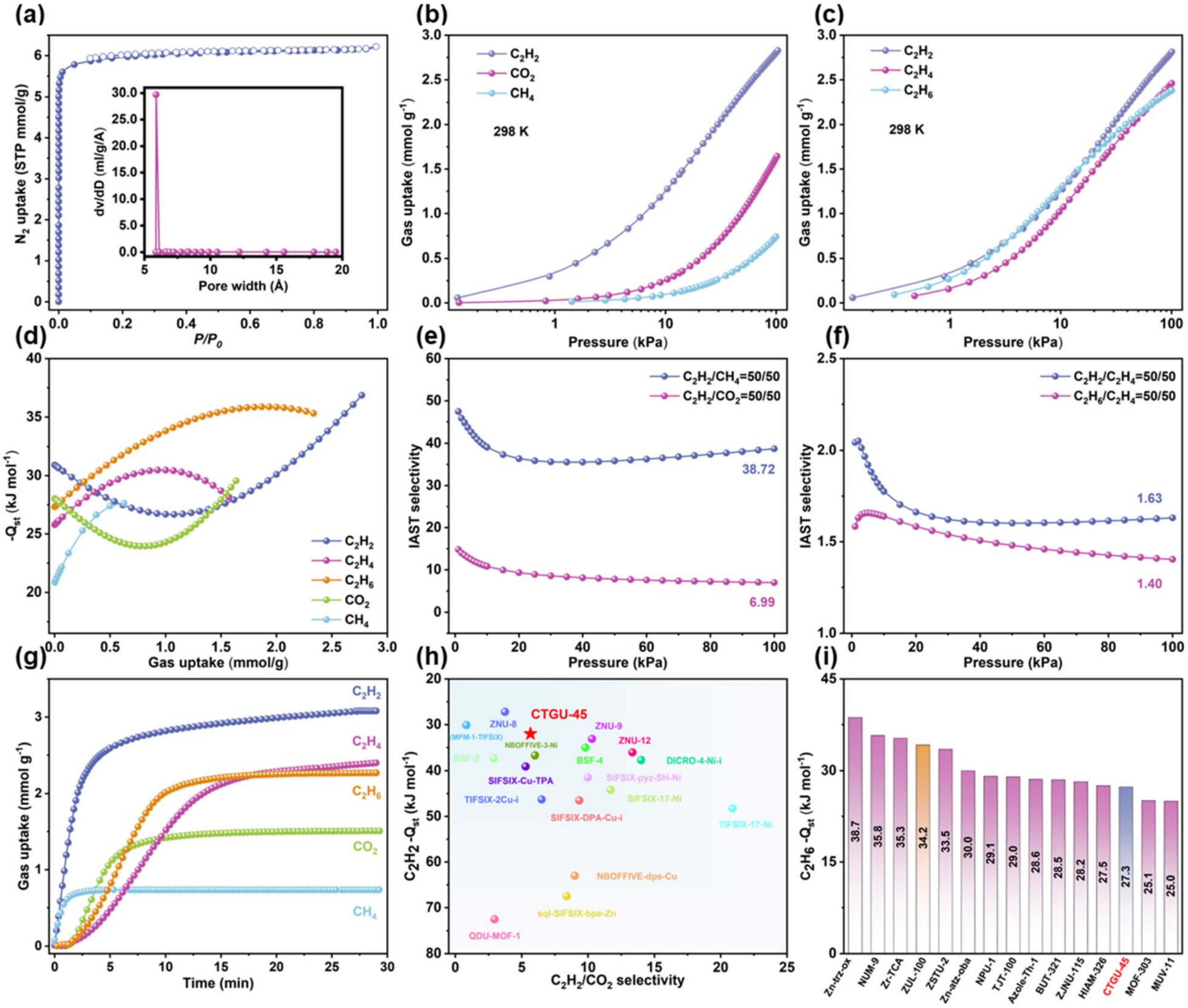

Fig. 2 (a) $N_2$ adsorption–desorption isotherms recorded at 77 K. The inset represents pore size distribution analyzed based on the H–K method. The single-component adsorption isotherms of (b) $C_2H_2$, $CO_2$, $CH_4$ and (c) $C_2H_2$, $C_2H_4$, $C_2H_6$ on CTGU-45 at 298 K. (d) Adsorption heats of $CH_4$, $CO_2$, and $C_2$ hydrocarbons. IAST selectivity of (e) $C_2H_2/CO_2$ (v/v, 50/50), $C_2H_2/CH_4$ (v/v, 50/50) mixtures and (f) $C_2H_2/C_2H_4$ (v/v, 50/50), $C_2H_6/C_2H_4$ (v/v, 50/50) mixtures at 298 K. (g) Adsorption kinetics profiles of CTGU-45 for $C_2H_2$, $C_2H_4$, $C_2H_6$, $CO_2$, and $CH_4$. (h) Comprehensive comparison of $C_2H_2/CO_2$ selectivity and $C_2H_2$-$Q_{st}$ value of CTGU-45 with the reported APMOFs. (i) A comparison of near-zero coverage isosteric heats for $C_2H_6$ among representative porous materials employed for one-step $C_2H_4$ purification from $C_2$ hydrocarbon mixtures.

diffusion rate of $C_2H_2$, $C_2H_4$, $C_2H_6$, $CO_2$, and $CH_4$ in CTGU-45. As shown in Fig. 2g, the time required to reach adsorption equilibrium follows the order: $T_{ads}$ ($CH_4$) < $T_{ads}$ ($C_2H_2$) < $T_{ads}$ ($CO_2$) < $T_{ads}$ ($C_2H_6$) < $T_{ads}$ ($C_2H_4$). In detail, the calculated diffusion time constants ($D_c/r_c^2$) of these gases on CTGU-45 are 0.0380 ($CH_4$), 0.2628 ($C_2H_2$), 0.0284 ($CO_2$), 0.0141 ($C_2H_6$), and 0.0104 s$^{-1}$ ($C_2H_4$), respectively (Fig. S29). Interestingly, in the desorption kinetics tests (Fig. S30), while $CH_4$ and $CO_2$ still exhibited the fastest desorption, the desorption rate sequence of the $C_2$ gases ($T_{des}$ ($C_2H_4$) < $T_{des}$ ($C_2H_6$) < $T_{des}$ ($C_2H_2$)) was exactly opposite to their respective adsorption rate sequence. This observation directly reflects the relative strength of their interactions with the framework, consistent with the assessments discussed earlier.

To further assess the separation potential of CTGU-45, the adsorption selectivity for equimolar $C_2H_2/CO_2$, $C_2H_2/CH_4$, $C_2H_2/C_2H_4$, and $C_2H_6/C_2H_4$ mixtures at 298 K was calculated based on the Ideal Adsorbed Solution Theory (IAST) after fitting isotherms to the single-site/dual-site Langmuir–Freundlich equation with excellent accuracy (Fig. S19–S23, $R^2 > 0.99999$). As illustrated in Fig. 2e and f, the IAST selectivity of CTGU-45 at 298 K and 101 kPa reached 6.99 for $C_2H_2/CO_2$ and 38.72 for $C_2H_2/CH_4$; notably, the selectivity for $C_2H_2/C_2H_4$ (50/50, v/v) (1.63) and $C_2H_6/C_2H_4$ (50/50, v/v) (1.40) further underscore its potential for one-step $C_2H_4$ purification. The $C_2H_2/CO_2$ selectivity is moderate among benchmark APMOFs, being comparable to those of NBOFFIVE-3-Ni (6.0) and TIFSIX-2-Cu-I (6.5), and higher than SIFSIX-Cu-TPA (5.3), QDU-MOF-1 (2.95), and ZNU-8 (3.74) (Fig. 2h). Meanwhile, the moderate $C_2H_2/CO_2$ selectivity, combined with the high $C_2H_2/CH_4$ selectivity, suggests that CTGU-45 is a viable candidate for separating $C_2H_2/CO_2$ and $C_2H_2/CH_4$ mixtures. Furthermore, the calculated $C_2H_2$ and $CO_2$ uptake (2.20 and 0.32 mmol $g^{-1}$) in the equimolar mixture closely matches the corresponding single-component adsorption capacities at 50 kPa (2.37 and 1.02 mmol $g^{-1}$), confirming the consistency between mixture prediction and gas adsorption measurement.

Grand Canonical Monte Carlo (GCMC) simulations and density functional theory with dispersion corrections (DFT-D) calculations were employed to elucidate the gas adsorption mechanisms in CTGU-45, revealing two primary binding sites within the framework: one near the $SiF_6^{2-}$ anion pillars and another inside the pore cavity (Fig. 3). In general, the region adjacent to the $SiF_6^{2-}$ pillars serves as a strong adsorption site for $CO_2$, $CH_4$, $C_2H_2$, and $C_2H_4$, whereas the pore cavity functions as the preferred strong binding region for $C_2H_6$. Taking $C_2H_2$ as a representative case, the first corresponds to a strong adsorption site, where the $C_2H_2$ molecule was confined by two $SiF_6^{2-}$ with a binding energy of −53.42 kJ $mol^{-1}$. Specifically, each H atom of $C_2H_2$ forms two C–H⋯F hydrogen bonds (H-bonds) with F atoms from two adjacent $SiF_6^{2-}$ pillars, resulting in a total of four H-bonds with distances ranging from 2.34 to 3.69 Å. These are complemented by C≡C⋯H interactions (distances: 2.58–3.45 Å) between the π-electrons of $C_2H_2$ and H atoms of imidazole rings. The second site corresponds to a weaker interaction environment within the pore cavity, involving C≡C⋯H (distances: 3.85–3.94 Å), C–H ($C_2H_2$)⋯N(imidazole) (2.91–3.82 Å), and C–H ($C_2H_2$)⋯π (imidazole/benzene) interactions with the distances of 3.10–3.92 Å. The binding energy for this weak-interaction site is −19.92 kJ $mol^{-1}$, substantially lower than that of the above-mentioned site. A similar distribution of adsorption sites was observed for $CO_2$, $CH_4$, and $C_2H_4$ with strong binding near the $SiF_6^{2-}$ pillars and weaker interactions in the pore cavity. For $CO_2$, the electronegative O atoms participated in C═O⋯H and C═O⋯N contacts with H and N atoms of the imidazole rings, as well as C═O⋯π interactions with the aromatic systems. Simultaneously, its electropositive C atom interacts with F atoms of the $SiF_6^{2-}$ pillars *via* O═C⋯F interactions. In the case of $CH_4$, $C_2H_4$, and $C_2H_6$, adsorption was governed by C–H⋯F and C–H⋯N interactions with the pillar F and imidazole N atoms, respectively, along with C–H⋯π contacts involving the aromatic rings of the TIB ligands. Notably, $C_2H_6$ exhibits its strongest adsorption within the pore cavity rather than near the anion pillars. Consequently, the binding energies of $CO_2$ and $CH_4$ at both types of adsorption sites are substantially lower than those of $C_2H_2$, while those of $C_2H_2$ and $C_2H_6$ are higher than those of $C_2H_4$. This energetic trend ($C_2H_2 > CO_2 > CH_4$; $C_2H_2 > C_2H_6 > C_2H_4$) further rationalizes the preferential adsorption of $C_2H_2$ over $CO_2$ and $CH_4$, and of $C_2H_2$ and $C_2H_6$ over $C_2H_4$ by CTGU-45. The stronger intermolecular interactions between the framework and $C_2H_2/C_2H_6$ directly correlate with its higher adsorption affinity, which is consistent with the observation on $Q_{st}$ and single-component adsorption data.

Dynamic breakthrough experiments were conducted to further evaluate the practical separation performance of CTGU-45 for $C_2H_2/CO_2$, $C_2H_2/CO_2/CH_4$, and $C_2$ hydrocarbon mixtures. As depicted in Fig. 4a, CTGU-45 can achieve efficient separation of a $C_2H_2/CO_2$ (50/50, v/v) mixture at a total gas flow rate of 4.0 mL $min^{-1}$, wherein $CO_2$ gases were detected in ∼9 min $g^{-1}$ while $C_2H_2$ breakthrough occurred at ∼22 min $g^{-1}$. Based on the integration of the curve, the dynamic $CO_2$ and $C_2H_2$ capture amounts of CTGU-45 were calculated to be 6.10 and 47.68 $cm^3$ $g^{-1}$, corresponding to approximately 26 and 90% of their respective static uptake values at 50 kPa (23.04 and 53.12 $cm^3$ $g^{-1}$), respectively. After adsorption saturation, the column was regenerated by purging with helium at 10 mL $min^{-1}$ under ambient temperature. The desorption profiles indicated rapid release of both gases, with $CO_2$ completely desorbed within 23 min $g^{-1}$. Beyond this point, high-purity $C_2H_2$ (>95.2%) was obtained at a productivity of 22.1 L $kg^{-1}$ (Fig. 4a). Subsequently, we further investigated the separation capacity of CTGU-45 for actual ternary $C_2H_2/CO_2/CH_4$ mixtures (33/33/33, v/v/v) with flow rates of 6 and 3 mL $min^{-1}$. Owing to its higher $C_2H_2$ uptakes and selectivity over $CO_2$ and $CH_4$, efficient separation of $C_2H_2$ from $C_2H_2/CO_2/CH_4$ mixtures can be fulfilled by CTGU-45 under different temperatures (298 and 308 K, Fig. S31).

As illustrated in Fig. 4b, $CH_4$ first eluted through the fixed bed at 3 min $g^{-1}$, followed by $CO_2$ at 4 min $g^{-1}$, whereas the $C_2H_2$ was retained in the packed column over 18 min $g^{-1}$. Despite $CO_2$ and $CH_4$ exhibiting a faster adsorption rate than $C_2H_2$ in CTGU-45, the stronger host–guest interactions between the framework and $C_2H_2$ (C–H⋯F, C–H⋯N, and C–H⋯π interactions) confer thermodynamic dominance in the actual separation process, leading to preferential $C_2H_2$ capture and the longest breakthrough time. The desorption curve further confirmed that polymer-grade $C_2H_2$ can be recovered at a productivity (>95.2%) of 19.7 L $kg^{-1}$.

For $C_2H_2/C_2H_4$ and $C_2H_6/C_2H_4$ mixtures with different compositions (50/50 or 10/90, v/v), $C_2H_4$ first eluted from the packed column while $C_2H_2$ or $C_2H_6$ remained strongly retained within the CTGU-45, demonstrating its ability to directly produce polymer-grade $C_2H_4$ products. In detail, $C_2H_4$ molecules broke through the fixed bed and were detected at 4.2 (3.7) and 42.9 (15.5) min $g^{-1}$ for the 50/50 (10/90) $C_2H_2/C_2H_4$ and $C_2H_6/C_2H_4$ mixtures, respectively, whereas $C_2H_2$ and $C_2H_6$ were adsorbed in the column over 51.7 (27.6) and 49.9 (51.4) min $g^{-1}$. As depicted in Fig. 4c and d, the productivity of 99.9% pure $C_2H_4$ from the 50/50 (10/90) $C_2H_2/C_2H_4$ and $C_2H_6/C_2H_4$ mixtures reached 28.6 (47.7) and 6.0 (33.3) L $kg^{-1}$, respectively. Building on the excellent separation performance observed for these binary mixtures, breakthrough experiments were further conducted using a ternary $C_2H_2/C_2H_6/C_2H_4$ (1/10/89, v/v/v) mixture. Notably, $C_2H_4$ eluted (0.9 min $g^{-1}$) prior to both $C_2H_2$ (1.8 min $g^{-1}$) and $C_2H_6$ (1.7 min $g^{-1}$), enabling the direct production of high-purity $C_2H_4$ (Fig. 4e). After calculation, 9.57 L $kg^{-1}$ of $C_2H_4$ with ≥99.95% purity can be directly obtained in a single cycle (298 K, 15 mL $min^{-1}$). For both ternary mixtures, CTGU-45 maintains reliable efficiency in $C_2H_2$ and $C_2H_4$ purification with steady gas productivities when the operating temperature is raised from 298 to 308 K, or when the flow rate is decreased from 6 to 3 mL $min^{-1}$ (15 to 14 mL $min^{-1}$, Fig. S31). Moreover, repeated breakthrough experiments over

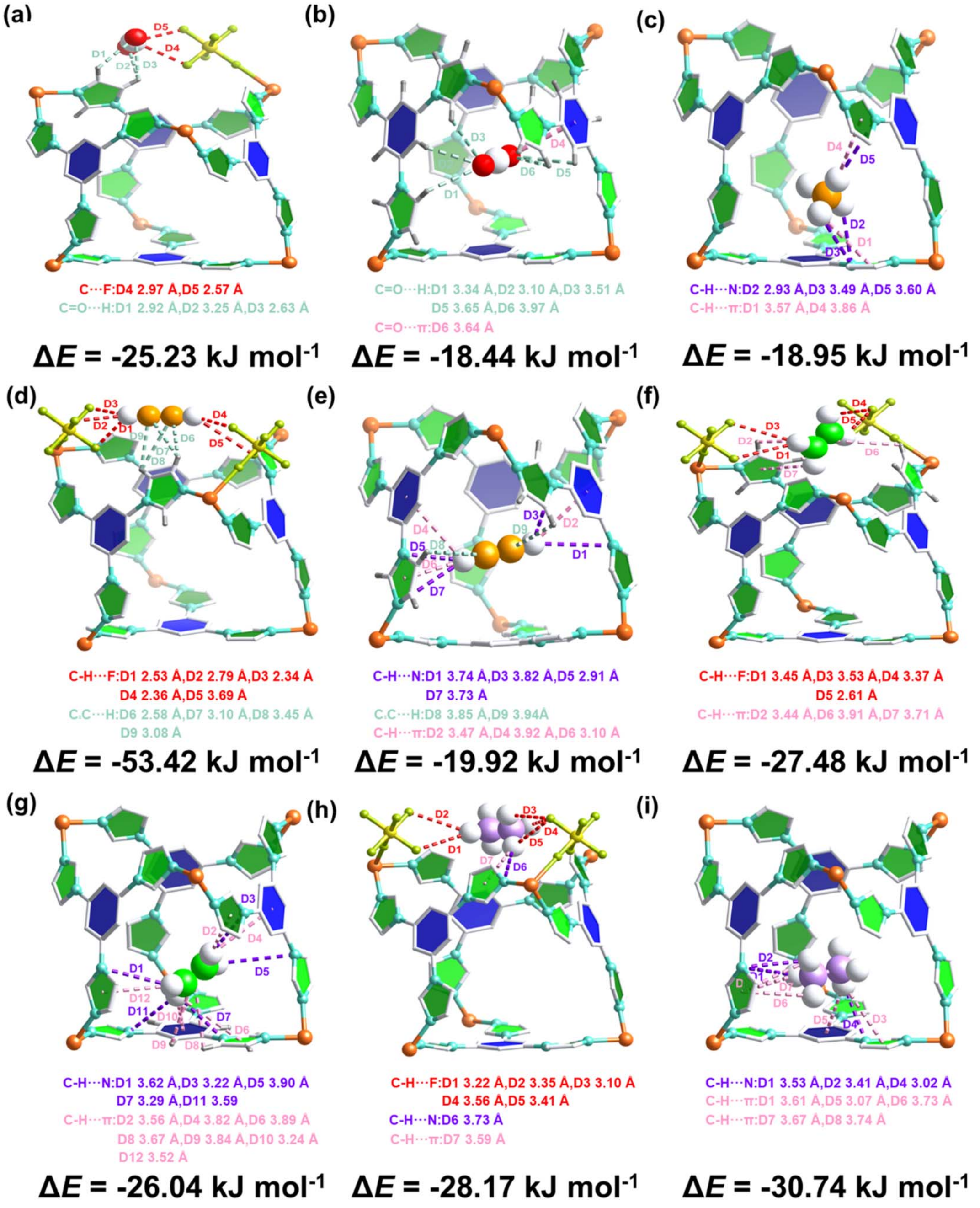

Fig. 3 Optimal binding sites and adsorption configurations of (a and b) $CO_2$, (c) $CH_4$, (d and e) $C_2H_2$, (f and g) $C_2H_4$, and (h and i) $C_2H_6$ molecules within CTGU-45 defined by DFT-D calculations.

five consecutive cycles showed no discernible decay in either $C_2H_4$ purity or productivity (9.24–11.0 L $kg^{-1}$), confirming the stable one-step $C_2H_4$ purification capability of CTGU-45 (Fig. 4f and S32). Finally, PXRD measurements reveal that CTGU-45 displays moderate chemical stability across a wide pH range (1–13) and in aqueous environments (Fig. S33). The combination of high separation efficiency, excellent adaptability, good thermal/chemical stability, and mild regeneration requirements (room-temperature He purging) underscores the potential of CTGU-45 for practical $C_2H_2$ and $C_2H_4$ purification.

In addition to the impressive separation properties, CTGU-45 crystals can be successfully synthesized at scale-up levels using glass containers with volumes ranging from 50 to 500 mL (Fig. 5a). PXRD measurements confirm the basic phase purity of the CTGU-45 sample obtained *via* scaled-up synthesis (Fig. 5b). Although the $N_2$ adsorption capacity of samples synthesized in 50, 100, and 200 mL vessels were only slightly lower than that of the 20 mL reference (Fig. 5c), and the sample prepared in a 500 mL bottle exhibits a 25.2% reduction in $N_2$ uptake. To further assess the impact on functional performance, $C_2H_2$ adsorption isotherms were measured at 298 K (Fig. 5d). The

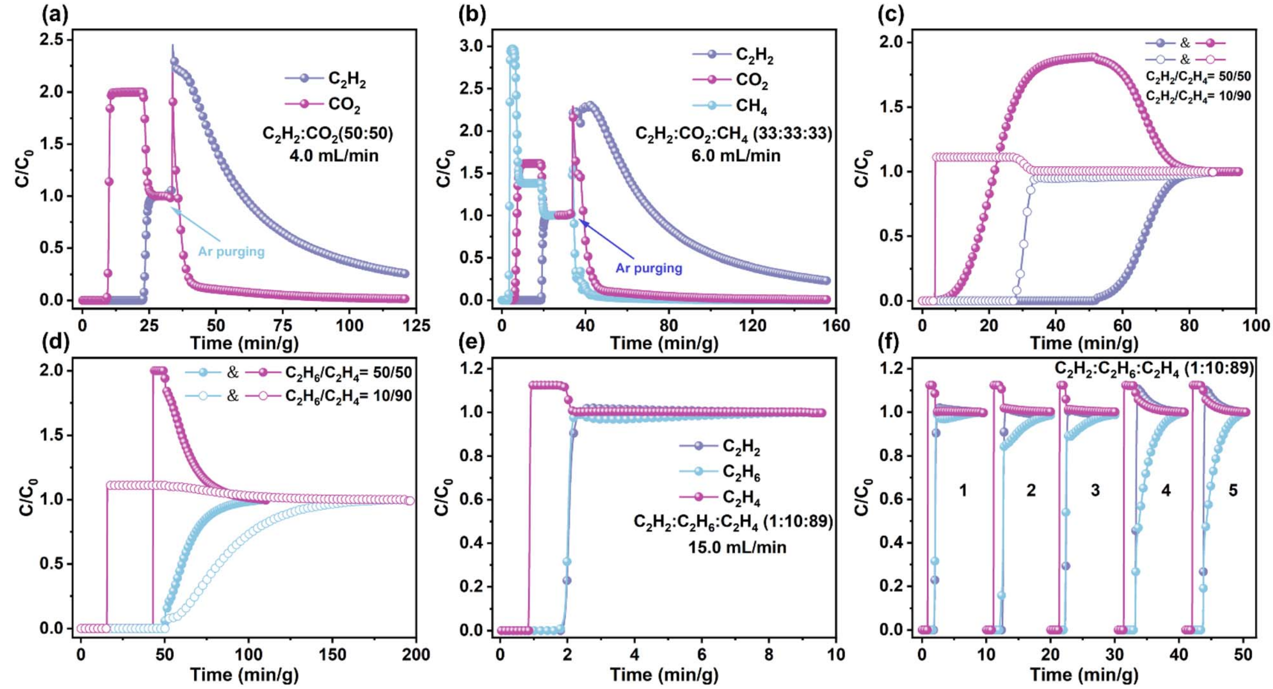

Fig. 4 Experimental column breakthrough curves and the desorption curves for (a) $C_2H_2/CO_2$ (50/50, v/v) and (b) $C_2H_2/CO_2/CH_4$ (33/33/33, v/v/v) on CTGU-45 at 298 K with a total flow of (a) 4 and (b) 6 mL $min^{-1}$. The dynamic breakthrough curves for (c) $C_2H_2/C_2H_4$ (50/50 and 10/90, v/v), (d) $C_2H_6/C_2H_4$ (50/50 and 10/90, v/v), and (e) $C_2H_2/C_2H_6/C_2H_4$ (1/10/89, v/v/v) on CTGU-45 at 298 K with a total flow of (c) 1, (d) 1, and (e) 15 mL $min^{-1}$. (f) Breakthrough cycling test of CTGU-45 for $C_2H_2/C_2H_6/C_2H_4$ (1/10/89, v/v/v, 298 K, 15 mL $min^{-1}$).

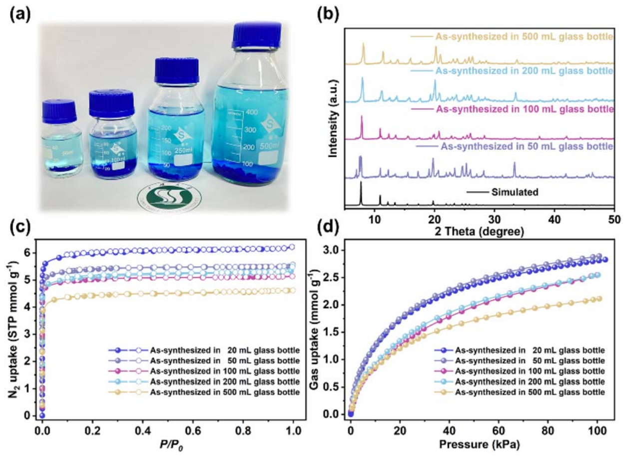

Fig. 5 (a) Scale-up synthesis of CTGU-45 at scales of 50, 100, 200, and 500 mL. (b) PXRD patterns, (c) $N_2$ adsorption–desorption isotherms, and (d) $C_2H_2$ adsorption isotherms of CTGU-45 synthesized at different scales *via* a solvothermal method.

results indicate that the $C_2H_2$ uptake of samples from 20 and 50 mL vessels is nearly identical, while those from 100 and 200 mL vessels show an approximate 8.8% decrease. In contrast, the sample synthesized in the 500 mL bottle exhibits a 25.4% reduction in $C_2H_2$ adsorption capacity, consistent with the trend observed in $N_2$ adsorption. Through additional analysis of the $N_2$ ads/des–orption isotherms, pore size distributions (Fig. S34), and PXRD patterns of samples synthesized at different scales, we found that the decrease in adsorption capacity may arise not only from undesired structural defects but also from the presence of by-products (amorphous, non-porous, and non-adsorbing). Since MOF synthesis is a complex self-assembly process governed by both thermodynamic and kinetic factors, changes in the scale of the reaction system—that is, the microscopic reaction conditions—can perturb the reaction pathway, leading to the formation of unknown by-products. To mitigate the formation of amorphous by-products and structural defects during industrial production for CTGU-45, future efforts might focus on two key strategies: (i) the implementation of continuous-flow synthesis or microwave-assisted heating can ensure uniform nucleation and growth conditions, thereby suppressing kinetic traps that lead to amorphous phases (ii) dynamic adjustment of reaction parameters (*e.g.*, reactant concentration, temperature gradients, local mass transfer); to steer the self-assembly toward the desired crystalline product.

## Conclusions

In summary, we reported a $SiF_6^{2-}$ embedded MOF, CTGU-45, featuring abundant electronegative F atoms and a low-polar cage environment, which enables one-step $C_2H_4$ purification *via* the simultaneous removal of $C_2H_2$ and $C_2H_6$. CTGU-45 exhibits high $C_2H_2$ and $C_2H_6$ uptake, markedly exceeding those for $CO_2$, $CH_4$, and $C_2H_4$. The low-polar pore environment effectively addresses the critical challenge of achieving $C_2H_6$-selective adsorption in $C_2H_6/C_2H_4$ separation, a behavior that is exceedingly rare among reported APMOFs. As a result, ~9.57 L $kg^{-1}$ of polymer grade $C_2H_4$ (≥99.95%) can be directly produced from ternary $C_2H_2/C_2H_6/C_2H_4$ (1/10/89, v/v/v) mixtures in a single step. DFT calculations reveal that strong C–H⋯F interactions between the inorganic $SiF_6^{2-}$ pillars and $C_2H_2$ enable CTGU-45 to not only efficiently purify $C_2H_2$ from $C_2H_2/CO_2/CH_4$ mixtures but also, in synergy with its $C_2H_6$-trapping capability, to achieve one-step production of high-purity $C_2H_4$ from ternary $C_2$ hydrocarbon mixtures. In addition, the low $C_2H_6$ $Q_{st}$ (27.3 kJ $mol^{-1}$) ensures facile regeneration with low energy input. Notably, CTGU-45 can be synthesized on a scalable level (up to 500 mL) with well-retained adsorption capacity. Overall, this work demonstrates that breaking ligand symmetry in APMOFs can fundamentally alter the spatial role of anion pillars, thereby reshaping pore surface chemistry and enabling rare one-step $C_2H_4$ purification from $C_2$ hydrocarbon mixtures.

## Author contributions

J.-J. Wu, P.-D. Zhang, X.-Q. Wu, and D.-S. Li conceived this project and designed the experiments. J.-J. Wu, S.-H. Huang, W.-W. Dong and Y.-P. Wu conducted the experiments. J.-J. Wu, P.-D. Zhang and X.-Q. Wu drafted the work. D.-S. Li revised and finalised the manuscript. All authors approved the submitted version.

## Conflicts of interest

There are no conflicts to declare.

## Data availability

The data that support the findings of this study are openly available in the supporting information (SI). Supplementary information: experimental procedures, TGA curves, gas adsorption/separation isotherms, crystallographic data, and theoretical computational details. See DOI: https://doi.org/10.1039/d6sc00819d.

CCDC 2522768 contains the supplementary crystallographic data for this paper.[42]

## Acknowledgements

We acknowledge the financial support from the National Natural Science Foundation of China (No. 22401172, No. 22371165), the 111 Project (D20015), the project of Hubei Three Gorges Laboratory (Z2022078, SK213002, SC232018, SC240013), Natural Science Foundation of Hubei Province (2024AFB021, 2022CFB326, Z2023203), Natural Science Foundation Innovation and Development Joint Fund of Hubei Province (2024AFD197).

## Notes and references

1 K. M. Carsch, H. Z. H. Jiang, R. A. Klein, A. S. Rosen, P. S. Summerhill, J. L. Peltier, A. J. Huang, R. A. Murphy, M. N. Dods, H. A. Silva, Z. Hasanbasri, H. Kwon, S. L. Karstens, Y. Yabuuchi, J. Börgel, J. W. Taylor, K. R. Meihaus, K. C. Bustillo, A. M. Minor, K. A. Persson, C. M. Brown, R. D. Britt, N. P. Stadie and J. R. Long, *Science*, 2025, **390**, 808–812.
2 I. J. Vitórica-Yrezábal, C. A. McAnally, M. P. Snelgrove, M. R. Warren, A. H. Hill, S. P. Thompson, M. Quinn, S. Mottley, S. Mottley, A. J. Fletcher and L. Brammer, *Nat. Chem.*, 2025, **17**, 1705–1711.
3 Z. Zhou, T. Ma, H. Zhang, S. Chheda, H. Li, K. Wang, S. Ehrling, R. Giovine, C. Li, A. H. Alawadhi, M. M. Abduljawad, M. O. Alawad, L. Gagliardi, J. Sauer and O. M. Yaghi, *Nature*, 2024, **635**, 96–101.
4 J.-W. Cao, S. Mukherjee, T. Pham, Y. Wang, T. Wang, T. Zhang, X. Jiang, H.-J. Tang, K. A. Forrest, B. Space, M. J. Zaworotko and K.-J. Chen, *Nat. Commun.*, 2021, **12**, 6507.
5 C. Lu, S. Liu, Z. Wang, X. Wei, X. Chen, X. Wang, J. Pang, S. Geng, X. Lu, J. Duan, F. Dai and X.-H. Bu, *Adv. Mater.*, 2025, **38**, e14488.
6 L. Li, R.-B. Lin, R. Krishna, H. Li, S. Xiang, H. Wu, J. Li, W. Zhou and B. Chen, *Science*, 2018, **362**, 443–446.
7 Y. Yang, L. Li, R.-B. Lin, Y. Ye, Z. Yao, L. Yang, F. Xiang, S. Chen, Z. Zhang, S. Xiang and B. Chen, *Nat. Chem.*, 2021, **13**, 933–939.
8 P. Ajayan, W. Wang, Y. Chen, X. Bu and P. Feng, *Adv. Mater.*, 2024, **36**, 2408042.
9 B. E. R. Snyder, A. B. Turkiewicz, H. Furukawa, M. V. Paley, E. O. Velasquez, M. N. Dods and J. R. Long, *Nature*, 2023, **613**, 287–291.
10 L. Li, L. Guo, D. H. Olson, S. Xian, Z. Zhang, Q. Yang, K. Wu, Y. Yang, Z. Bao, Q. Ren and J. Li, *Science*, 2022, **377**, 335–339.
11 G.-R. Si, X.-J. Kong, L.-H. Xie, Y.-T. Zhang, T. He and J.-R. Li, *Sci. Bull.*, 2025, **70**, 3475–3478.
12 Z.-H. Guo, L.-Q. Yang, Q.-G. Zhai, G.-P. Yang and Y.-Y. Wang, *Angew. Chem., Int. Ed.*, 2025, **64**, e202519278.
13 L. Wang, H. Chen, C. Lou, G. Xiong, Y. Jiang, B. Chen and Y. Zhang, *Angew. Chem., Int. Ed.*, 2025, **64**, e202519160.
14 Z.-S. Wang, M.-Y. Zhou, D.-Y. Hu, X.-X. Chen, J.-X. Chen, X.-W. Zhang, D.-D. Zhou, J.-P. Zhang and X.-M. Chen, *J. Am. Chem. Soc.*, 2025, **147**, 47977–47984.
15 Y. Xiao, A. N. Hong, Z. Jia, X. Bu and P. Feng, *J. Am. Chem. Soc.*, 2025, **147**, 42786–42795.
16 T. Wu, D. Zhou, Z. Yang, Y. Liu, P. Yin, K. Lu, F. Jiang, X. Suo, L. Yang, X. Cui and H. Xing, *J. Am. Chem. Soc.*, 2025, **148**, 5299–5306.
17 Z. Ji, Y. Zhou, C. Chen, D. Yuan, M. Wu and M. Hong, *Angew. Chem., Int. Ed.*, 2024, **63**, e202319674.
18 Y. Jiang, Y. Hu, B. Luan, L. Wang, R. Krishna, H. Ni, X. Hu and Y. Zhang, *Nat. Commun.*, 2023, **14**, 401.
19 A. Cadiau, K. Adil, P. M. Bhatt, Y. Belmabkhout and M. Eddaoudi, *Science*, 2016, **353**, 137–140.
20 F. Zheng, L. Guo, R. Chen, L. Chen, Z. Zhang, Q. Yang, Y. Yang, B. Su, Q. Ren and Z. Bao, *Angew. Chem., Int. Ed.*, 2022, **61**, e202116686.
21 X. Cui, K. Chen, H. Xing, Q. Yang, R. Krishna, Z. Bao, H. Wu, W. Zhou, X. Dong, Y. Han, B. Li, Q. Ren, M. J. Zaworotko and B. Chen, *Science*, 2016, **353**, 141–144.

22 H.-M. Wen, C. Liao, L. Li, L. Yang, J. Wang, L. Huang, B. Li, B. Chen and J. Hu, *Chem. Commun.*, 2019, **55**, 11354–11357.
23 M. Lusi, P. B. A. Fechine, K.-J. Chen, J. J. Perry and M. J. Zaworotko, *Chem. Commun.*, 2016, **52**, 4160–4162.
24 H. Li, C. Liu, C. Chen, Z. Di, D. Yuan, J. Pang, W. Wei, M. Wu and M. Hong, *Angew. Chem., Int. Ed.*, 2021, **60**, 7547–7552.
25 M. Shivanna, K.-i. Otake, B.-Q. Song, L. M. van Wyk, Q.-Y. Yang, N. Kumar, W. K. Feldmann, T. Pham, S. Suepaul, B. Space, L. J. Barbour, S. Kitagawa and M. J. Zaworotko, *Angew. Chem., Int. Ed.*, 2021, **60**, 20383–20390.
26 M.-Y. Gao, A. A. Bezrukov, B.-Q. Song, M. He, S. J. Nikkhah, S.-Q. Wang, N. Kumar, S. Darwish, D. Sensharma, C. Deng, J. Li, L. Liu, R. Krishna, M. Vandichel, S. Yang and M. J. Zaworotko, *J. Am. Chem. Soc.*, 2023, **145**, 11837–11845.
27 H. S. Scott, M. Shivanna, A. Bajpai, D. G. Madden, K.-J. Chen, T. Pham, K. A. Forrest, A. Hogan, B. Space, J. J. Perry Iv and M. J. Zaworotko, *ACS Appl. Mater. Interfaces*, 2017, **9**, 33395–33400.
28 H. Chen, Y. He, Y. Han, J. Hu, J. Li, Y. Jiang, B. Keshta, L. Wang and Y. Zhang, *Chin. J. Struct. Chem.*, 2025, **44**, 100508.
29 Y. Zhang, J. Hu, R. Krishna, L. Wang, L. Yang, X. Cui, S. Duttwyler and H. Xing, *Angew. Chem., Int. Ed.*, 2020, **59**, 17664–17669.
30 L. Wang, W. Sun, Y. Zhang, N. Xu, R. Krishna, J. Hu, Y. Jiang, Y. He and H. Xing, *Angew. Chem., Int. Ed.*, 2021, **60**, 22865–22870.
31 H.-Y. Li, Z.-Z. Xue, S.-D. Han, G.-M. Wang and T. He, *Sep. Purif. Technol.*, 2025, **357**, 130094.
32 K.-J. Chen, H. S. Scott, D. G. Madden, T. Pham, A. Kumar, A. Bajpai, M. Lusi, K. A. Forrest, B. Space, J. J. Perry and M. J. Zaworotko, *Chem*, 2016, **1**, 753–765.
33 Y. Zhang, W. Sun, B. Luan, J. Li, D. Luo, Y. Jiang, L. Wang and B. Chen, *Angew. Chem., Int. Ed.*, 2023, **62**, e202309925.
34 Y. Zhang, Y. Han, B. Luan, L. Wang, W. Yang, Y. Jiang, T. Ben, Y. He and B. Chen, *J. Am. Chem. Soc.*, 2024, **146**, 17220–17229.
35 P. S. Nugent, V. L. Rhodus, T. Pham, K. Forrest, L. Wojtas, B. Space and M. J. Zaworotko, *J. Am. Chem. Soc.*, 2013, **135**, 10950–10953.
36 S. Mukherjee, N. Kumar, A. A. Bezrukov, K. Tan, T. Pham, K. A. Forrest, K. A. Oyekan, O. T. Qazvini, D. G. Madden, B. Space and M. J. Zaworotko, *Angew. Chem., Int. Ed.*, 2021, **60**, 10902–10909.
37 N. Kumar, S. Mukherjee, N. C. Harvey-Reid, A. A. Bezrukov, K. Tan, V. Martins, M. Vandichel, T. Pham, L. M. van Wyk, K. Oyekan, A. Kumar, K. A. Forrest, K. M. Patil, L. J. Barbour, B. Space, Y. Huang, P. E. Kruger and M. J. Zaworotko, *Chem*, 2021, **7**, 3085–3098.
38 T. Wu, C. Yu, R. Krishna, Z. Qiu, H. Pan, P. Zhang, X. Suo, L. Yang, X. Cui and H. Xing, *AIChE J.*, 2024, **70**, e18312.
39 S.-Q. Yang, F.-Z. Sun, P. Liu, L. Li, R. Krishna, Y.-H. Zhang, Q. Li, L. Zhou and T.-L. Hu, *ACS Appl. Mater. Interfaces*, 2021, **13**, 962–969.
40 H.-G. Hao, Y.-F. Zhao, D.-M. Chen, J.-M. Yu, K. Tan, S. Ma, Y. Chabal, Z.-M. Zhang, J.-M. Dou, Z.-H. Xiao, G. Day, H.-C. Zhou and T.-B. Lu, *Angew. Chem., Int. Ed.*, 2018, **57**, 16067–16071.
41 P.-D. Zhang, X.-Q. Wu, Q. Shuai, J. Yu, X. Zhang and J.-R. Li, *ACS Mater. Lett.*, 2024, **6**, 4632–4638.
42 CCDC 2522768: Experimental Crystal Structure Determination, 2026, DOI: 10.5517/ccdc.csd.cc2qp4m6.